ELSEVIER

Contents lists available at ScienceDirect

Physics of the Earth and Planetary Interiors

journal homepage: www.elsevier.com/locate/pepi





Detecting low-latitude outer core-surface waves with 25 years of satellite secular variation data

Carla R. Grüne ^a, Kathryn A. Whaler ^a, Frederik Dahl Madsen ^{a,b},

- ^a The University of Edinburgh, School of GeoSciences, Grant Institute, Edinburgh, EH9 3FE, United Kingdom
- ^b British Geological Survey, Lyell Centre, Research Avenue, Edinburgh, EH14 4BA, United Kingdom

ARTICLE INFO

Keywords: Geomagnetism Core-surface flow modelling Core-surface waves Satellite magnetism

ABSTRACT

Fluid motion in the Earth's liquid outer core generates most of the geomagnetic field, and its time changes over timescales of one year or longer, the secular variation (SV). Data from the satellite missions Ørsted, CHAMP, CryoSat-2 and Swarm, together with data from ground observatories, were combined to yield a SV dataset spanning from late 1997 to early 2023. These SV data were inverted for time-varying core surface fluid velocity assuming it is purely advective, with the main field specified by the CHAOS-7.16 field model. The inversion was regularised both in time and in space. In time, the difference in velocity between individual epochs was minimised. In space, small-scale velocity structures were penalised. Flow acceleration was then calculated from first differences of velocities at successive epochs. Time-longitude diagrams of azimuthal acceleration show sloping features at low latitudes, interpreted as signatures of propagating waves. Waves propagating both eastwards and westwards were observed, with propagation velocities of approximately 1700 km/yr which is in agreement with previous inferences of fast core waves. Power spectral density plots reveal that the energy is concentrated in modes with periods of 6-7 years, and azimuthal wavenumbers -5, -2 and 2, where negative wave numbers indicate westward motion. There is a higher energy content in the westward propagating waves than in those travelling eastwards. Finally, we find intermittent low-latitude standing waves, which coincide with times of recent equatorial geomagnetic jerks, consistent with inferences of magneto-Coriolis and Alfvén waves from other studies.

1. Introduction

The Earth is pervaded by its magnetic field, the largest part of which is generated by the motion of fluid in the Earth's outer core. Here, a mixture of predominantly iron and nickel convects vigorously within the rapidly rotating regime of the Earth and, by stretching and advecting the magnetic field lines contained within it, acts against the decay of the field through Ohmic dissipation (Gubbins and Roberts, 1987). Together with diffusion, the fluid movement also produces the time changes of the field over durations of a year or longer, called the secular variation (SV).

Based on kinematic arguments, the effect of magnetic diffusion should be negligible except at short lengthscales on timescales of centuries and shorter (Roberts and Scott, 1965), such that the core fluid can be treated as a perfect electrical conductor. This leads to the "frozen-flux" approximation (Alfvén, 1942) whereby magnetic field lines are tied to fluid parcels. Hence magnetic field lines act as tracers of the fluid flow, and it is possible to image the flow in the outer

core just underneath the core-mantle boundary (CMB). The role of diffusion has been further investigated in dynamo models, where it plays an active role near the CMB (Tsang and Jones, 2024). Still for the radial component of the induction equation at the core surface, advection appears to dominate in comparison to diffusion over a wide range of timescales (Barrois et al., 2017; Aubert and Gillet, 2021). Assuming negligible magnetic diffusion, the relationship between the radial component of the magnetic field (B), B_r , the radial component of the SV ($\dot{\mathbf{B}}$), $\partial B_r/\partial t$, and the horizontal flow \mathbf{u}_h at the CMB (assumed perfectly spherical and concentric to the Earth's surface) is described by the radial component of the frozen-flux magnetic induction equation:

$$\frac{\partial B_r}{\partial t} = -\nabla_H \cdot (\mathbf{u}_h B_r) \tag{1}$$

where $\nabla_H = \nabla - \hat{\mathbf{r}} (\hat{\mathbf{r}} \cdot \nabla)$. The magnetic field and SV at the CMB cannot directly be observed. However, by assuming the mantle to be electrically insulating and thus free of magnetic field sources, it is possible to downward-continue measurements made either at the

E-mail addresses: s243220@dtu.dk (C.R. Grüne), Kathy.Whaler@ed.ac.uk (K.A. Whaler), f.d.madsen@sms.ed.ac.uk (F.D. Madsen).

^{*} Corresponding author.

 $^{^{1}\,}$ Now at the Danish Technical University, 2800 Kongens Lyngby, Denmark.

Earth's surface or above, e.g., at satellite height (e.g. Holme, 2015). We consider the radial component of the induction equation because only the radial magnetic field and SV components are continuous across the electrical conductivity jump at the CMB, and can hence be related to the flow (e.g. Bloxham and Jackson, 1991).

The launch of the Swarm satellite mission in late 2013 was the continuation of an era of satellite magnetic field observations, almost continuously monitoring the geomagnetic field from space since the launch of the Ørsted satellite in 1999 (Friis-Christensen and Lühr, 2006). The satellite missions have significantly improved the spatial coverage of the field, as compared to ground observatories which provide continuous monitoring in time, but are unevenly distributed in space. This improved coverage has enabled observation of rapid (on timescales of a few years or longer) variations of the main field (e.g. Lesur et al., 2022), often linked to rapidly evolving flows in the core which are superimposed on a more slowly evolving, eccentric, planetary-scale fluid circulation, the so-called planetary gyre (Pais and Jault, 2008; Finlay et al., 2023).

These rapid changes in the magnetic field or in inferred flow patterns have been interpreted as the signatures of hydromagnetic waves travelling through the outer core (e.g. Gillet et al., 2022). Observing and identifying the different types of waves may provide further understanding about the leading order force balances, and we may consequentially gain insight into the governing physical processes inside the core (Finlay, 2008). A variety of wave types including magneto-Archimedes-Coriolis (MAC), Rossby and magneto-Coriolis can be generated by a combination of Coriolis, magnetic and buoyancy (Archimedean) forces. Buoyancy forces could be important if there is density stratification beneath the CMB (e.g. Buffett, 2014; Buffett et al., 2016), and the occurrence of mid- to high-latitude wave-like patterns has been tentatively interpreted as the signature of this (Chi-Durán et al., 2021). At lower latitudes, magneto-Coriolis waves have been identified by e.g. Gerick et al. (2021) and Gillet et al. (2022).

Hydromagnetic waves have further been connected to geomagnetic jerks, the fastest observable changes in the Earth's core field (e.g. Aubert and Finlay, 2019). Geomagnetic jerks were first observed as "V-shapes" in SV vector components measured at ground observatories, separating regions of otherwise almost linearly evolving SV (Courtillot and Mouël, 1984). These abrupt changes in the evolution of the SV are one of the main hurdles to longer-term (on the timescales of years) forecasting of the Earth's magnetic field behaviour (e.g. Aubert et al., 2022). In the geomagnetic satellite era, 7 geomagnetic jerks, with a 3–4 year spacing between them, were recorded: in 1999 (Mandea et al., 2000), 2003 (Olsen and Mandea, 2007), 2007 (Chulliat et al., 2010), 2011 (Chulliat and Maus, 2014), 2014 (Torta et al., 2015), 2017 (Whaler et al., 2022) and 2020 (Pavón-Carrasco et al., 2021). Madsen et al. (2025) hypothesise an 8th geomagnetic jerk in the equatorial Pacific in 2024.

It is widely accepted that jerks have an internal origin (Malin and Hodder, 1982), and they are commonly traced back to processes inside the outer core (Jackson et al., 2015). They are associated with localised pulses in the secular acceleration (SA) (e.g. Chulliat et al., 2010), or even pulses in azimuthal core-surface flow acceleration (Gillet et al., 2019; Kloss and Finlay, 2019; Gillet et al., 2022; Li et al., 2024; Madsen et al., 2025). These pulses are likely driven by core-surface waves (e.g. Gillet et al., 2022; Li et al., 2024). However, it remains clear that in this framework, jerks are connected to the sign changes of the acceleration – geomagnetic (e.g. Chulliat and Maus, 2014) or core-surface flow (e.g. Madsen et al., 2025) – between successive, opposite-polarity pulses.

The SA and the flow acceleration are closely related, as can be seen by taking the first time derivative of Eq. (1) (e.g. Lesur et al., 2010; Pinheiro et al., 2019; Lesur et al., 2022; Aubert et al., 2022):

$$\ddot{B}_r = -\dot{\mathbf{u}}_h \cdot \nabla_H B_r - B_r \nabla_H \cdot \dot{\mathbf{u}}_h - \mathbf{u}_h \cdot \nabla_H \dot{B}_r - \dot{B}_r \nabla_H \cdot \mathbf{u}_h \tag{2}$$

where \ddot{B}_r is the radial component of the SA, \ddot{B} , and \dot{u} is the flow acceleration. The first two terms on the right-hand side of Eq. (2)

describe how the flow acceleration interacts with the magnetic field to generate a SA signature.

Both geomagnetic jerks and the arrival of hydromagnetic waves from deeper within the core at its surface have been connected to rapidly occurring, high-amplitude SA features (e.g. Chulliat and Maus, 2014; Aubert and Finlay, 2019) and signals in the flow acceleration, suggesting it is worthwhile to further investigate flow acceleration. Furthermore, rapid propagation such as that associated with hydromagnetic waves may be more easily detected in the flow acceleration, as taking the time derivative filters out the more slowly evolving flow believed to be responsible for longer-period processes. Determining core surface flow acceleration from SV data from the Swarm mission, Whaler et al. (2022) found high-amplitude features travelling azimuthally at velocities of approximately $900 \; \mathrm{km} \; \mathrm{yr}^{-1}$ at low latitudes, but were unable to extract the associated periods and wavenumbers due to the short timespan of the dataset. Gillet et al. (2022) found similar low-latitude features in observation-based core flow velocity profiles, travelling westwards at velocities of $\sim 1500 \text{ km yr}^{-1}$.

We utilise 25 years of satellite data to investigate waves in the coresurface flow acceleration. We combine satellite SV observations from the Ørsted, CHAMP, CryoSat-2, and Swarm missions, additionally supplemented with ground observatory measurements, to create a dataset spanning about 25 years, from late 1997 to the start of 2023. Using the prior assumptions that the flow has a large scale spatial structure and exhibits only minimal change with time, we invert this dataset for core surface velocity and, from it, determine flow acceleration. The latter is then used to detect features indicative of waves propagating beneath the CMB.

In the following, first, the data used and then the methods applied to determine the flow velocity and acceleration profiles are outlined in Section 2. In Section 3, we present the results, and subsequently discuss them in Section 4. Lastly, in Section 5, we draw our conclusions.

2. Data and methods

2.1. Data

The SV dataset, spanning from 1997.67 to 2023.00, is comprised of (r, θ, ϕ) component values, where r is radially outwards, θ is colatitude and ϕ is longitude, from the Ørsted, CHAMP, CryoSat-2 and Swarm satellite missions, together with a continuous series of the same vector component observations from 186 ground magnetic observatories. Their time distribution is shown in Fig. 1.

We use geomagnetic virtual observatories (GVOs) introduced by Mandea and Olsen (2006) to represent the satellite SV data. GVO data are produced from satellite magnetic measurements using the updated methodology of Hammer et al. (2021), and comprise vector geomagnetic field time series as if observed by a grid of regularly spaced, stationary observatories at satellite height. Annual first differences of main field values provide the SV. We use GVO time series with 4-month sampling from all four satellite missions, together with their error estimates for each component, computed using the variance of residuals between the GVO datum and its CHAOS 7.16 model estimate.

The ground observatory values are based on hourly means from which external fields have been removed, using an improved model of the magnetospheric ring current (Olsen et al., 2014). Robust means are calculated over the same 4-month intervals as the GVOs, and annual first differences provide the resultant SV time series. Their uncertainties are calculated in the same way as for the GVOs.

These SV time series are input directly into the inversion for core flow, following e.g. Whaler (1986) and Beggan and Whaler (2008), rather than inverting spherical harmonic coefficients of the SV obtained from them. This means that any misfit between data and model predictions is from the modelling strategy adopted, and is not potentially impacted by how well the SV spherical harmonic model fitted the observations. These previous studies inferred successive snapshots of

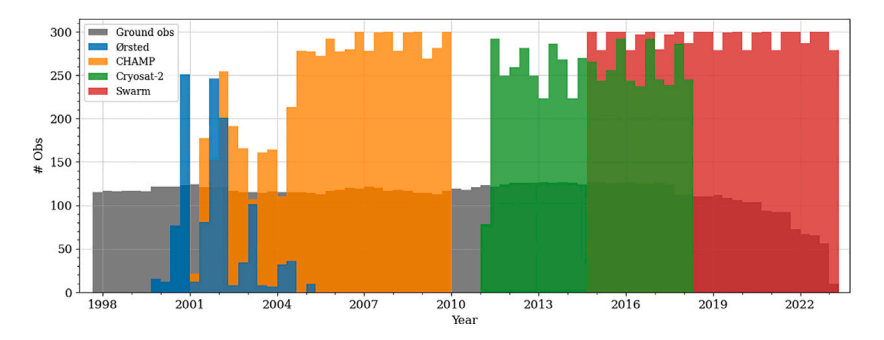


Fig. 1. Number of observation points in each 4-month bin from the different data sources.

the core flow covering the duration of the data, rather than a time dependent model as is obtained here. Another approach using data rather than spherical harmonic models of them is to co-estimate the time dependent main field and core surface flow directly from main field observations such as in the studies of Lesur et al. (2010), Lesur et al. (2015) and Bärenzung et al. (2018). Alternative methods include using a reduced stochastic model that replicates the spatiotemporal statistics of geodynamo simulations to guide the inversion from main field and SV observations (e.g. Istas et al., 2023).

2.2. Flow inversion

When modelling the core-surface flow, we assume that the fluid in the outer core is incompressible and may thus be decomposed into the sum of its toroidal and its poloidal components, \mathbf{u}_t and \mathbf{u}_s (e.g. Roberts and Scott, 1965). At the CMB, the toroidal part wraps around the core surface where it takes on the form of eddies and gyres, and it is responsible for the overall westward drift (e.g. Holme, 2015; Suttie et al., 2025). Poloidal flow is the part of the flow associated with overturning motion; signatures of such up- and downwellings at the CMB have been interpreted as an indicator of convection reaching all the way to the CMB (Whaler, 1980). The general expression for the flow, expressed in terms of the toroidal and poloidal scalar fields \mathcal{T} and \mathcal{S}_t , is

$$\mathbf{u} = \mathbf{u}_t + \mathbf{u}_s = \nabla \times (\mathcal{T}\mathbf{r}) + \nabla \times \nabla \times (\mathcal{S}\mathbf{r}). \tag{3}$$

We note here that at the CMB, the radial component of the flow vanishes, and the second term on the right-hand side of Eq. (3) becomes $\nabla_H(rS)$. The toroidal and poloidal scalar potentials can be expanded in spherical harmonics:

$$\mathcal{T} = \sum_{l=1}^{\infty} \sum_{m=0}^{l} P_l^m (\cos \theta) \left[t_l^{mc} \cos m\phi + t_l^{ms} \sin m\phi \right]$$
 (4)

$$S = \sum_{l=1}^{\infty} \sum_{m=0}^{l} P_l^m (\cos \theta) \left[s_l^{mc} \cos m\phi + s_l^{ms} \sin m\phi \right]$$
 (5)

where the P_l^m are Schmidt quasi-normalised associated Legendre functions of degree l and order m, and the t_l^{mc} , t_l^{ms} , s_l^{mc} and s_l^{ms} are the flow potential coefficients. The scalar potentials representing ${\bf B}$ and $\dot{{\bf B}}$ can also be expanded in spherical harmonics; Equation (1) can then be manipulated to yield a set of linear equations relating the spherical harmonic coefficients of the SV, the magnetic field and the flow potentials through Gaunt and Elsasser integrals (e.g. Whaler, 1986).

We then use the expressions for the SV data components in terms of their spherical harmonic coefficients to relate them to the flow coefficients. This gives the set of linear equations directly relating the flow, represented by its poloidal and toroidal potential coefficients, to observations of the SV, which can be written

$$\mathbf{d} = \mathbf{A}\mathbf{m} \tag{6}$$

where d is a vector of SV observations, m contains the spherical harmonic flow coefficients and A is the so-called equations of condition

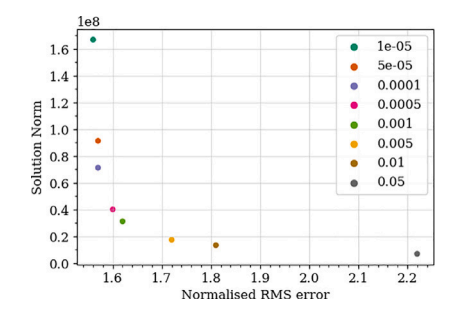


Fig. 2. Trade-off between solution norm value and normalised data misfit, used to determine the value of the spatial damping parameter.

matrix relating the two. A depends on a model of B_r (e.g. Whaler, 1986; Beggan and Whaler, 2009), here specified by the CHAOS-7.16 magnetic field model (Finlay et al., 2020) and truncated at spherical harmonic degree and order 14. We solve this linear inverse problem to obtain m.

The problem of estimating the horizontal flow at the top of the outer core from SV observations using Eq. (1) is non-unique. In order to calculate a unique solution, we thus rely on making assumptions on the flow prior to inversion (e.g. Holme, 2015). Here, we apply damping both in space and time. In space, we assume that the flow is large scale. Penalising small-scale flow features has the advantage of simplicity, both in its imposition and in the resulting flow, but it is a strong a priori constraint: studies with stochastic priors suggest small-scale features should be considered (e.g. Gillet et al., 2015; Baerenzung et al., 2016), and in geodynamo simulations they (together with small-scale magnetic field features) are responsible for a significant component of the SV (e.g. Schwaiger et al., 2024). Furthermore, Eymin and Hulot (2005) show that the SV generated by interaction of the large-scale magnetic field with the small-scale flow we neglect (as well as by the large-scale flow interacting with the small-scale magnetic field obscured by the crustal field) can be significant. Other commonly made assumptions on the spatial flow structure, for example that the flow is quasi-geostrophic (Pais and Jault, 2008) or columnar (Amit and Olson, 2004), require the flow to be symmetric about the equator. Compared to these, our assumption has the advantage that it does not constrain the flow geometry beyond requiring it to be large scale, and allows for equatorial asymmetry if required by the data. To penalise small-scale structures, we apply the so-called 'strong norm' (Bloxham, 1988) which minimises the second spatial derivatives of the velocity components over the core surface:

$$\oint_{\Omega} \left(\left(\nabla_{H}^{2} u_{\theta} \right)^{2} + \left(\nabla_{H}^{2} u_{\phi} \right)^{2} \right) \mathrm{d}\Omega \tag{7}$$

where Ω is the CMB.

We express the time dependence of the flow by computing its toroidal and poloidal scalar coefficients (Eqs. (4) and (5)) at discrete

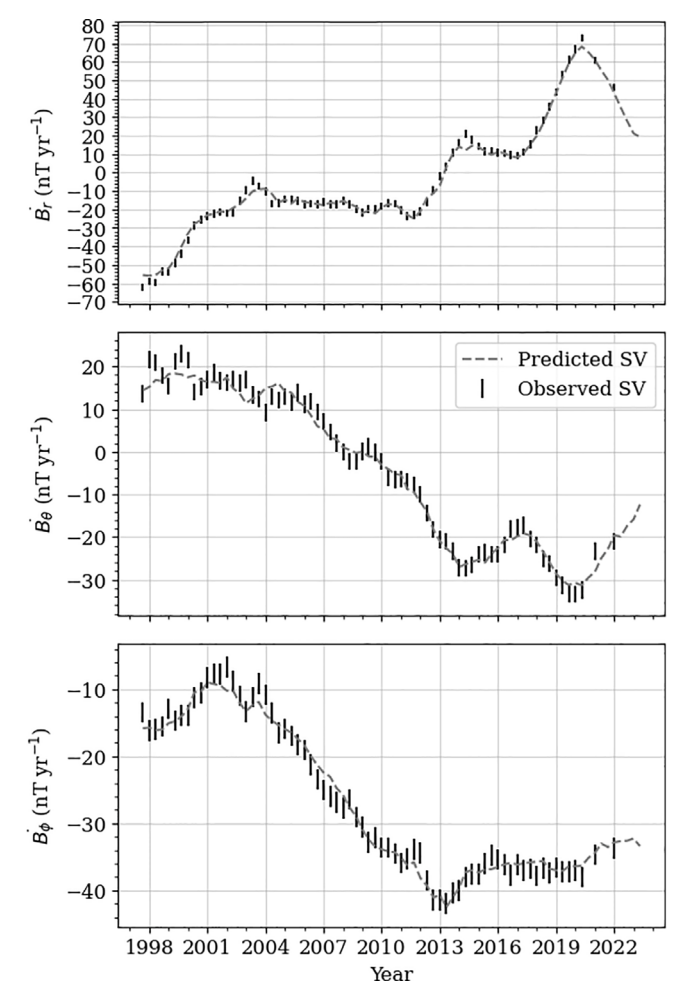


Fig. 3. Observed and predicted SV time series at ground observatory GUA (13.6°N,144.9°E). Error bars are one standard deviation.

time points spaced 4 months apart (at the same times as we have SV data). The inversion is then regularised in time by minimising the first differences between the velocity coefficients of successive epochs as described by Whaler et al. (2016), thus effectively minimising the flow acceleration. We therefore invert all the data simultaneously for a time dependent flow.

Applying both the temporal and spatial damping, a model of the flow coefficients, $\hat{\mathbf{m}}$, is obtained as (e.g. Whaler et al., 2016, 2022):

$$\hat{\mathbf{m}} = (\mathbf{A}^T \mathbf{C}_e \mathbf{A} + \lambda_v \mathbf{C}_m^{-1} + \lambda_t \mathbf{D}^T \mathbf{D})^{-1} \mathbf{A}^T \mathbf{C}_e \mathbf{d}.$$
 (8)

Here, C_e is the covariance matrix of the SV data, assumed independent from each other, making C_e diagonal. C_m is the *a priori* covariance matrix, whose elements are determined from the spatial norm given by Eq. (7), and whose contribution is controlled by the size of the spatial damping parameter λ_v . D^TD is the temporal damping matrix (explicit expression given by Whaler et al. (2016)), whose contribution is controlled by the size of the temporal damping parameter λ_v .

The trade-off curve (Fig. 2) visualises the relationship between the spatial complexity of the resultant flow (given by Eq. (7)) and the misfit between the (normalised) data and model predictions, as a function of λ_v . From this curve, we determined the damping parameter resulting in a good balance between the two to be 5×10^{-3} . The temporal damping parameter λ_t was set to 1000, following Whaler et al. (2016). Flow coefficients in Eqs. (4) and (5) were estimated up to spherical harmonic degree and order 20, sufficient to ensure convergence.

2.3. Acceleration

From the flow velocity model, flow acceleration is calculated by taking the first differences of the spherical harmonic flow coefficients, u, and dividing by the timestep between epochs, δt :

$$\dot{u} = \frac{u_t - u_{t-1}}{\delta t} \tag{9}$$

Here, \dot{u} are the spherical harmonic flow acceleration coefficients, and $\delta t = 4$ months.

In order to extract and investigate any periodicity in the accelerations, we computed the power spectral density (PSD) of its azimuthal component. For this, we follow the approach of Wheeler and Kiladis (1999) as applied by Finlay (2005). The azimuthal acceleration component, re-gridded into longitude-time data frames, is first detrended in time at each location. We tested the impact of either removing the mean value (over the time series), or removing the best-fit linear trend, following Whaler et al. (2022); we find both produce very similar results. Results shown here are after removing the best-fit linear trend.

After detrending, the individual time series are tapered at the beginning and end using a cosine function, to prevent ringing. The values are then zero-padded at the start and the end of the time series, and subjected to a two-dimensional fast Fourier transform. The PSD is the sum of squares of the real Fourier coefficients as a function of frequency.

3. Results

3.1. Flow

The resultant flow has a normalised root-mean-square (rms) misfit between data and model predictions of 1.71. A value above the target of 1 may arise from a combination of data uncertainties being underestimated, remaining external field contamination in the data, neglect of diffusion, and adopting a simple flow modelling strategy. Comparisons between the flow-predicted SV and both satellite observations and ground observatory data at the ground observatory GUA and a nearby GVO, both in the west Pacific, are shown in Figs. 3 and 4; they show that the model predictions follow the observations closely throughout the timespan studied. At times where observations are more scattered, predictions vary more and the misfit is larger (see for example B_{θ} between 2011 and 2013 in Fig. 4); where observations are less scattered, as particularly during the Swarm era, predictions and observations match well.

The energies within both the toroidal and poloidal flow components converge rapidly as a function of spherical harmonic degree, as enforced by the chosen spatial norm (Fig. 5). We note here that the flow is predominantly toroidal. Most of the toroidal energy is in spherical harmonic degree 1 - associated with westward drift - until 2010, where spherical harmonic degree 2 becomes dominant. Around the same time, in the poloidal flow energy, we see an increase in spherical harmonic degree 3, which continues until 2023. These changes indicate a redistribution of energy in the large-scale flow over the past 20 years. Fig. 6 shows an example snapshot of the flow from epoch 2018.33. It displays the expected features associated with the planetary-scale eccentric gyre (Pais and Jault, 2008): strong westward drift underneath the Atlantic hemisphere at low latitudes turns into poleward flow beneath North America. Underneath the Bering Strait, it concentrates into the high-amplitude jet along the tangent cylinder (e.g. Livermore et al., 2017). Under East Asia, it flows south towards the equator again, where it re-organises into the Atlantic westward flow band. This largescale pattern is seen consistently throughout the entire time span, with little structural change. The figure also shows concentrated eastward drift underneath the equatorial Pacific after 2011 (as also observed by e.g. Whaler et al. (2022), Ropp and Lesur (2023), Finlay et al. (2023), Madsen et al. (2025), Rogers et al. (2025)).

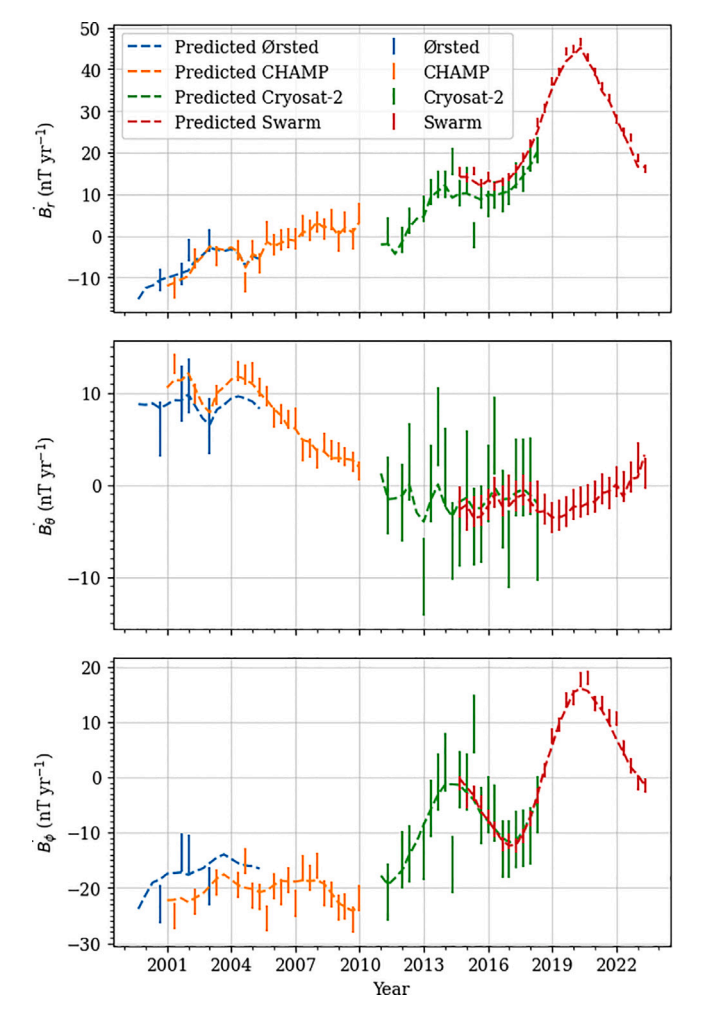


Fig. 4. Observed and predicted SV time series at GVO at $(6.0^{\circ}N,164.4^{\circ}E)$. Error bars are one standard deviation. The mode prediction for each satellite is evaluated at its corresponding altitude (measured here in distance from the centre of the Earth): Ørsted: 7126.2 km; CHAMP: 6741.2 km; Cryosat-2: 7098.2 km; and Swarm: 6861.2 km.

Superimposed on the flow in Fig. 6 is the poloidal flow potential, S, which indicates regions of divergent (S > 0) and convergent (S < 0) flow. We can thus use S as a proxy for regions of up- and downwelling (e.g. Whaler, 1980). We see that there is an up- and downwelling pattern associated with the high latitude jet underneath the Bering Strait, which is not mirrored in the southern hemisphere. There is also a region of strong flow convergence underneath the western equatorial Pacific, where the equatorial Atlantic westward flow meets the equatorial Pacific eastward flow. Eastward flow beneath the low-latitude Pacific is sourced from an upwelling beneath Indonesia and downwelling underneath Central America. In a numerical geodynamo simulation, Aubert et al. (2022) find upwelling and downwelling patches at the CMB to be the result of shallow convective bursts, providing a possible mechanism for our observations. In addition to this large-scale, steady pattern, some more rapid flow changes occur. A video of the core-surface flow from 1997 to 2023 is provided in the supplementary material. Over the period between 2001 and 2004, a counter-clockwise eddy forms beneath the South Indian Ocean, then disappears again in 2011-2012, as a result of its western half stretching out to the west. This variation is similar to that reported by Whaler et al. (2016) who found a counter-clockwise eddy at the same location in flow models computed from observatory monthly means, although their eddy appears and disappears twice in the time interval studied, in both instances over timescales of months.

Under the Pacific hemisphere, there are no structural changes to the flow pattern visible until 2010, which marks the beginning of a period of increased dynamics in this region. Most notably, between 2010 and 2014, a low-latitude patch of flow between about 160°E and 180°E changes direction from westwards to eastwards, and remains stably eastwards after, which is associated with the concentration of the upwelling region at these longitudes. A patch of flow divergence located at about (20°N, 200°E), that had persisted stably (with slight drifting) prior to this vanishes.

Fig. 7 shows the root-mean-square (rms) velocity of our flow as a function of time. The global flow speed is variable throughout the past 25 years, with an overall increasing trend from around 10 km yr⁻¹ to 11 km yr⁻¹. These values are in agreement with other studies (e.g. Lesur et al., 2015; Gillet et al., 2022; Ropp and Lesur, 2023). Fig. 7 furthermore shows the decomposition of the flow into commonly inspected flow statistics. Our flow has only ~15% poloidal energy, and is predominantly tangentially geostrophic and symmetric about the equator, with around 20-25% of its energy in the ageostrophic and asymmetric components, as found in previous studies (e.g. Whaler, 1986; Bloxham, 1992; Beggan and Whaler, 2008). This is noteworthy as our flow is not bound by any geometrical assumptions, such as quasi-geostrophy, nor is it influenced by any dynamo priors through data-assimilation. This dominance of tangential geostrophy and equatorial symmetry is thus a direct requirement of an acceptable fit to the data, rather than an implication of our modelling choices. Finally, we also see that the proportion of energy represented by the zonal toroidal coefficients has decreased by 20% over the past 20 years. These coefficients are associated with changes in length-of-day (e.g. Jault et al., 1988; Jackson, 1997; Jault and Finlay, 2015). Changes in the zonal part of the flow over timescales like those we observe have been proposed to result from convective flows (More and Dumberry, 2018), or as signatures of MAC waves in the presence of a stably stratified layer beneath the CMB (Buffett, 2014).

3.2. Flow acceleration

Here we investigate the azimuthal flow acceleration only, hence all mentions of flow acceleration hereafter refer to this component. A snapshot is shown in Fig. 8. (Its values are considerably larger than those reported by Whaler et al. (2022), who applied the same inversion technique to spatial gradient SV GVO values from the Swarm era; owing to a numerical error, their values are a factor 3 too small). We observe some localised, anomalously high-amplitude acceleration pulses. Reaching amplitudes up to twice those of the background, they tend to appear at mid-to-low latitudes and, at most times, underneath the Indian Ocean, the Atlantic, or, especially after 2010, the west Pacific. These pulses appear and disappear over the course of months and, in some instances, appear to be drifting along the core surface. At several times, transitions between two opposite-polarity pulses coincide with assigned timings of geomagnetic jerks. For instance, a negative pulse that had existed under the mid-Pacific since mid-2015 vanishes at the beginning of 2017, then re-appears with opposite polarity in late 2017, the transition is coincident with the 2017 Pacific jerk (Whaler et al., 2022). This positive peak then becomes weaker in early 2020 and, in late 2020, is eventually replaced by a negative one propagating in from the west: a jerk in the Pacific area around the onset of 2020 was reported by Pavón-Carrasco et al. (2021). The left-hand-side of Fig. 9 shows a longitude-time section of the azimuthal acceleration at 10°N. Here, east-west movement of the pulses is particularly apparent. Its east-most section, spanning from 0° to about 100°E, has low amplitude, and is relatively featureless. By contrast, the section spanning the region between about 120°E to 240°E (corresponding approximately to the Pacific region), has areas of very high acceleration amplitudes. Alternating negative and positive acceleration features form patterns of sloping stripes, interpreted as eastward propagation of high-amplitude spots in a region around 120°E (tentatively, since

Toroidal coefficients

Poloidal coefficients

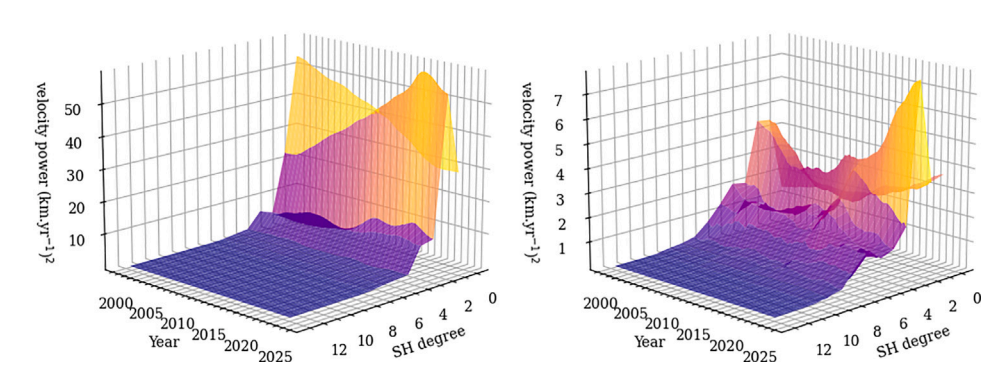


Fig. 5. Power spectrum of toroidal (left) and poloidal (right) flow coefficients up to spherical harmonic degree 14, as a function of time and degree. Values above spherical harmonic degree 14 are negligibly small, and thus not shown here. The colour indicates velocity power, as given by the *z*-axis. Note that the *z*-axes scales differ by an order of magnitude between toroidal and poloidal flow coefficients.

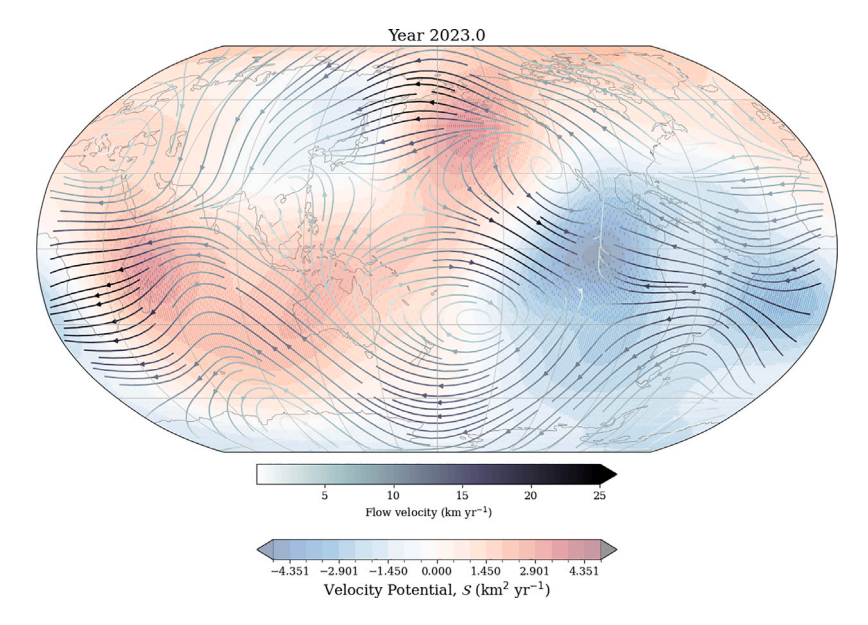


Fig. 6. Snapshot of the flow in 2023 superimposed on the poloidal velocity potential, S, which is associated with up- (S > 0) and downwelling (S < 0). Plot is centred at 180° longitude in Robinson projection. Continents are shown for reference only.

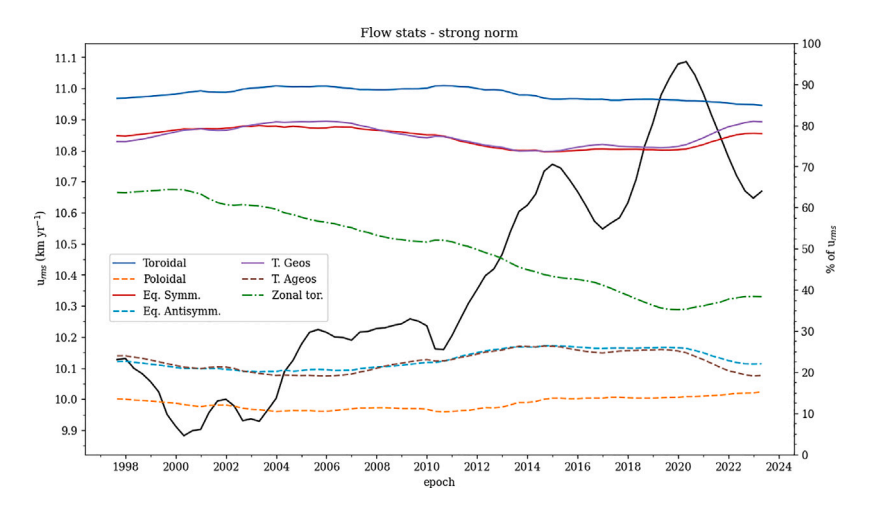


Fig. 7. Root-mean-square (rms) velocity, and percentage spatial statistics of flow as a function of time. Black line shows rms velocity (left axis) and coloured lines show percentage decomposition (right axis). Note that each colour represents a different part of the flow, that both the rms velocity and its proportional parts are evaluated at each epoch. Abbreviations: Eq. Symm. – Equatorially symmetric; T. Geos – Tangentially geostrophic; Eq. Antisymm. – Equatorially antisymmetric; T. Ageos – Tangentially ageostrophic; Zonal tor – Zonal toroidal.

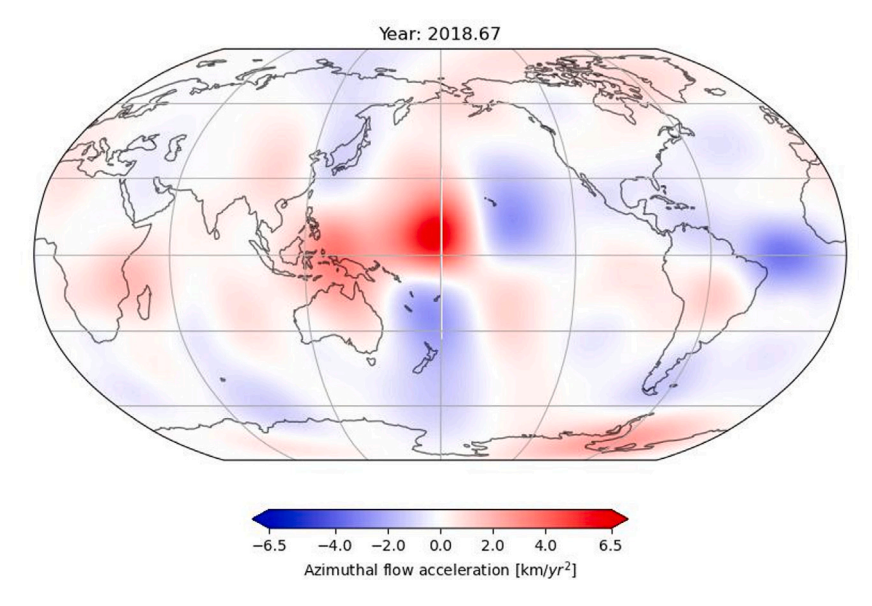


Fig. 8. Snapshot of the CMB azimuthal flow acceleration at epoch 2018.67. Underneath the Pacific and the Atlantic, high-amplitude pulses appear at low latitudes. Robinson projection with continents shown for reference only.

the pattern only appears over a narrow band of longitude), and, with larger amplitude, westward movement east of 150°E. The former only appears around 2015, the latter becomes well defined around 2010 and remains throughout the rest of the interval studied. Fitting a straight line to the slope of the westward propagating features yields an approximate propagation velocity of 1700 km yr⁻¹, significantly faster than the typical fluid flow velocities. A similar pattern can be seen in a third section between 250°E and 330°E (i.e., roughly the Atlantic region), separated from section two by a narrow quiescent strip. Here, signals appear earlier in time, and weaken significantly after 2017. Interestingly, the ~3 year time intervals between these systematic sign changes of the acceleration correspond broadly with the time interval between geomagnetic jerks, the approximate timings of which are marked on the diagram as grey, dashed lines. We chose the line placements on the plot as suggested by the acceleration sign changes, in accordance with occurrence time intervals reported for each jerk (see Chulliat et al. (2010), Chulliat and Maus (2014), Torta et al. (2015), Whaler et al. (2022), Pavón-Carrasco et al. (2021)). At our chosen latitude, some jerks only appear in the flow acceleration either in the Atlantic or the Pacific hemisphere. Furthermore, the timing of jerks as suggested by the acceleration signals are slightly different in the two hemispheres. This differential delay in jerk-arrival times has been attributed to the electrical conductivity structure of the mantle (e.g. Pinheiro and Jackson, 2008; Pinheiro et al., 2011), but has also been hypothesised to arise from the geometry of the main field at the CMB (see for instance Aubert et al. (2022)).

The PSD corresponding to this longitude-time section is shown on the right-hand-side of Fig. 9. Note that all PSD plots presented here are cropped from below and above to include only signals with periods well within the time span studied, and resolved by the frequency of sampling. Upper limits are chosen either based on possible time resolution or on the frequency content of the signal shown. At 10°N, the PSD plot shows the strongest peak at wavenumber –2 and a period of about 6 years, matching well the results obtained by Gillet et al. (2022). Weaker peaks are seen at wavenumbers –5, –4, and 2 at the same period. Negative wavenumbers correspond to westward travelling modes, whereas positive wavenumbers indicate eastward travelling.

To see whether this signal is regionally limited, the analysis was repeated at different latitudes. The left-hand side of Fig. 10 shows longitude-time diagrams at the equator and a selection of latitudes north of it, including 10°N. The longitude-time section at the equator shows features like those seen at 10°N. North of 10°N, these features

become weaker until they eventually vanish at mid-latitudes. At $60^{\circ}N$, rapidly alternating, high-amplitude features appear early on in the time series. Note that at these early times, fewer satellite data are available, putting more weight on the ground observatory data (see Fig. 1 for the data distribution through time). Endpoint effects from the temporal damping may also affect the first (and last) few epochs. Besides the sparsity of high latitude observatories, measurements towards the poles are more contaminated by external field effects. Hence it is possible that these rapid, high-amplitude features are a data artefact.

In the corresponding PSDs, on the right-hand side of Fig. 10, focused spectral peaks appear at low latitudes and lose energy quickly when moving to higher latitudes, such that at 20°N, only a faint signal is left, which then vanishes further north. Between the equator and 10°N, there is some change in the energy content and position of the individual modes, most notably the movement of one peak centre from wavenumber –4 at the equator to –5 at 10°N, accompanied by a small increase in the energy, while other modes lose energy. Overall, however, the general PSD morphology is very similar at the two locations. In the southern hemisphere (not shown), the development is similar: the signal loses energy with increasing distance from the equator, although more quickly than in the north.

The time evolution of the PSD at $10^\circ N$, obtained by repeating the above analysis on overlapping intervals of length 10 years, is shown in Fig. 11. The interval length of 10 years was chosen as it is longer than the period of the signals, yet still allows enough time windows to resolve some time variation. This sub-division shows that the energy focusing seen previously persists through the entire time span studied. The general signal remains broadly constant across the individual time intervals, while displaying small changes in the morphology and exact location of the peaks. Earlier, the signal is noisier and contains less energy. At later times, when more and higher-quality data are used (Fig. 1), the signal becomes more focussed and its energy content increases. There is some shift in the locations of the peaks between wavenumbers; for instance, the peak initially localised at wavenumber -3 moves to -2 in 2005, where it remains thereafter.

A latitude-time section along the line of constant longitude 170°E is shown in the left-hand side of Fig. 12. At low to mid-latitudes, a very systematic pattern of alternating positive-negative signatures emerges after approximately 2011: two high-amplitude patches appear, positioned above each other and opposite in sign, covering latitudes from about 25°S to 15°N and separated by a quiescent strip which remains at approximately the same latitude of $\sim\!5^\circ\mathrm{S}$ throughout. They

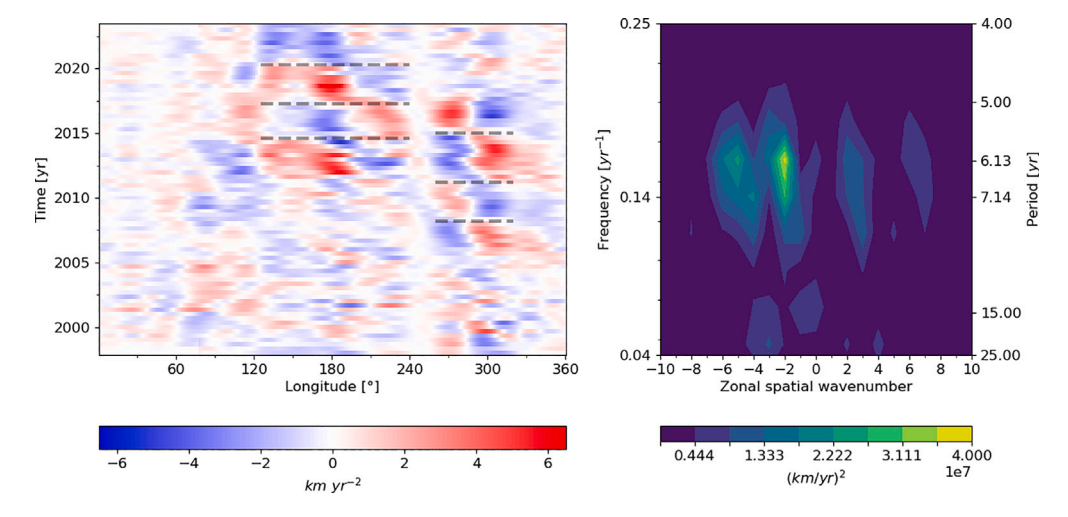


Fig. 9. Left-hand side: longitude-time section of azimuthal core surface flow acceleration at 10°N. The dashed lines indicate timings of the 2007, 2011, 2014, 2017 and 2020 geomagnetic jerks, the exact placements in time are as suggested by the flow acceleration polarity switches. RHS: corresponding power spectral density. Negative wavenumber peaks indicate westward movement, positive peaks eastward movement.

swap polarity approximately every 3 years. In general (see Figure A.1 for other longitudes), the axis of anti-symmetry in the azimuthal acceleration is at approximately the latitude of the CMB magnetic equator, which may provide clues to the physical nature of the oscillation. Between 2013 and 2018, the two positive acceleration patches connect across the normally quiescent band to form a sloping feature, suggesting latitudinal movement.

A further pattern is visible in the latitude-time section at high latitudes: between approximately 55°N and 70°N, a single strip of high-amplitude acceleration appears, reversing polarity more rapidly than that seen at low latitudes. After about 2007, this signal becomes much less distinct. Note, as for the high-latitude signal shown before in Fig. 10, that this signal could be an artefact of the poorer-quality data available at high latitudes earlier in the timeseries.

The right-hand side panel of Fig. 12 shows the PSD corresponding to the time-latitude section on the left-hand side. Note that here, PSD peaks at negative wave numbers correspond to northwards-travelling signals, peaks at positive wave numbers to southward travelling ones. The PSD again shows distinct peaks. Two modes with periods between 6 and 7 years have wave numbers ± 6 , suggesting that the signal appearing in the time-latitude diagram is a standing wave. Here, the southward travelling mode has a slightly shorter period and slightly increased energy content compared to the northward travelling one. The angular dimension associated with these peaks is approximately 30°, or, taking as outer core radius 3485 km, a length scale of 1825 km. This length scale matches approximately the latitudinal width of the low-latitude signal visible in the time-latitude section on the left-hand panel; the signal width might appear slightly larger, but it is difficult to determine the exact edges by inspection. Two more peaks are located at wavenumbers -2 and 4, at similar periods of between 20 and 25 years. Because these durations are close to the length of the data time series, however, they should be interpreted with caution. Lastly, another, minor peak appears with a period of about 3.5 years and wavenumber 2. Although the period of this peak is similar to that of the high-latitude signal, the associated angular dimension of 90° does not suggest connection of the peak to the signal.

The pattern observed at $170^{\circ}E$ is not representative of the whole core surface. At different longitudes (see Figure A.1), the time-latitude sections show periodic patterns of different morphologies, strengths, and extent in time; in some places, no coherent signal appears at all. Corresponding PSDs behave accordingly, indicating again superposition of north-south propagating modes in some places, and no or weaker signals in other locations.

4. Discussion

The SV predicted by the flow model matches both the satellite and ground observatory observations; is also reproduces the sharp changes associated with geomagnetic jerks (Figs. 3 and 4). The predicted SV follows observations very closely when they are not very scattered. which is especially evident after the launch of the Swarm mission in 2013. At times when observations are more scattered, flow predictions are more varied but still follow the general pattern. Overall, the flow predictions match the SV observations well, confirming that we found a model that is in good agreement with the data. The flow features resemble those in previous studies. We image the planetary-scale eccentric gyre (Pais and Jault, 2008; Finlay et al., 2023) including the region of accelerating fluid flow near the tangent cylinder underneath the Bering Strait (Livermore et al., 2017; Bärenzung et al., 2018; Gillet et al., 2019). Our acceleration is more subtle, as the jet speed never exceeds 22 km yr⁻¹ (see Figure A.3), similar to the value found by Bärenzung et al. (2018) but considerably less than 40 km yr⁻¹ found by Livermore et al. (2017) and Gillet et al. (2019). (Note that Bärenzung et al. (2018) present average values of the toroidal flow strength, rather than of the azimuthal component of the total flow, but as the flow is predominantly toroidal and, in this region, predominantly azimuthal, their values should be representative.) In agreement with Gillet et al. (2019), the jet speed starts to decline in 2016. In the southern hemisphere, our jet is weak, accelerating steadily from around 8 km yr⁻¹ to 14 km yr⁻¹ (Figure A.3); Livermore et al. (2017), Bärenzung et al. (2018) and Gillet et al. (2019) find values in the range 10-25 km yr⁻¹, with no pronounced acceleration. These differences highlight the effect of model choices on the details of the flow. The more variable flow in the Pacific region after 2010, particularly the switch from westward to eastward flow around 2010, is consistent with that reported by Ropp and Lesur (2023), the latter was also noted by e.g. Gillet et al. (2019), Rogers et al. (2025) and Madsen et al. (2025).

Localised high-amplitude flow acceleration features in the equatorial region such as those found here have previously been identified in observation-based models (Kloss and Finlay, 2019; Madsen et al., 2025) and simulations of the geodynamo and the core flow field (Aubert and Finlay, 2019; Aubert et al., 2022). Both time-longitude (Fig. 9) and latitude-time (Fig. 12) slices as well as the corresponding PSDs reveal systematic, rapidly propagating, periodic patterns in the azimuthal flow acceleration, and suggest an underlying wave structure. The comparisons between PSDs of longitude-time sections at different latitudes (Fig. 10) show that the periodic signals become weaker (dropping by an order of magnitude over 20° latitude) and less sharp towards

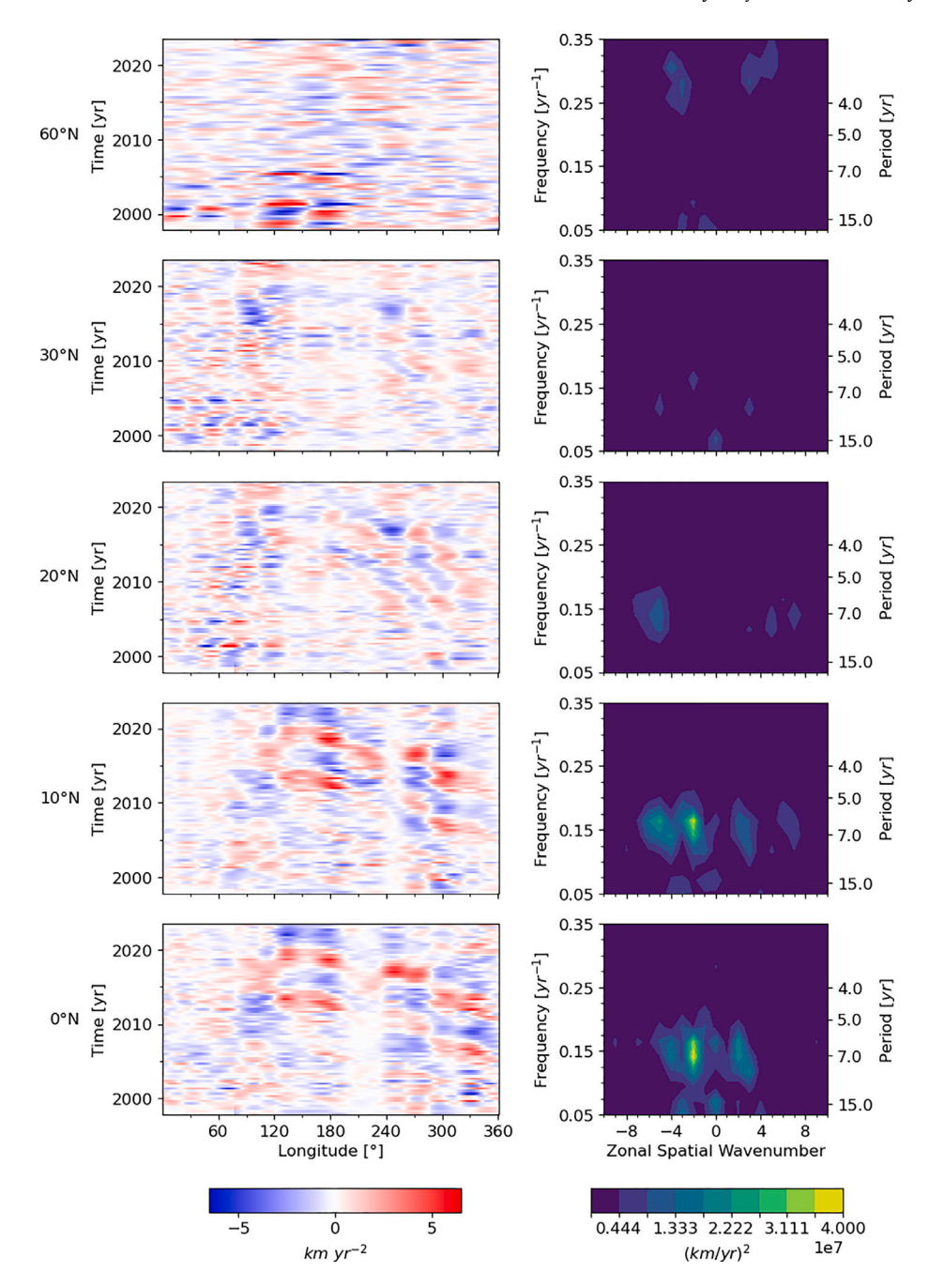


Fig. 10. Latitudinal variations of longitude-time diagrams (left-hand side panels) and corresponding power spectral densities (right-hand side panels) of the azimuthal core surface flow acceleration at a selection of northern hemisphere latitudes.

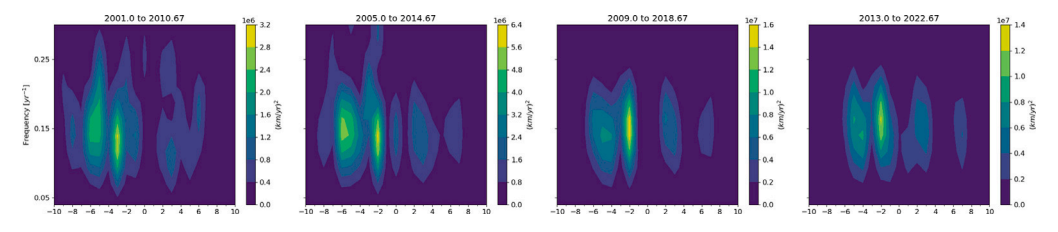


Fig. 11. Time evolution of the power spectral density at 10° N. The time intervals are sliding windows, start and end times of each interval are indicated above each panel.

mid- and high latitudes, indicating a focusing at equatorial and low latitudes (with the exception of the high-amplitude feature beneath Alaska). Gillet et al. (2024) and Rogers et al. (2025) reported patterns

in longitude-time diagrams of the azimuthal flow velocity component at the equator similar to those we find at the equator (Fig. 10). Both of these studies find rapid, azimuthally propagating, polarity-alternating

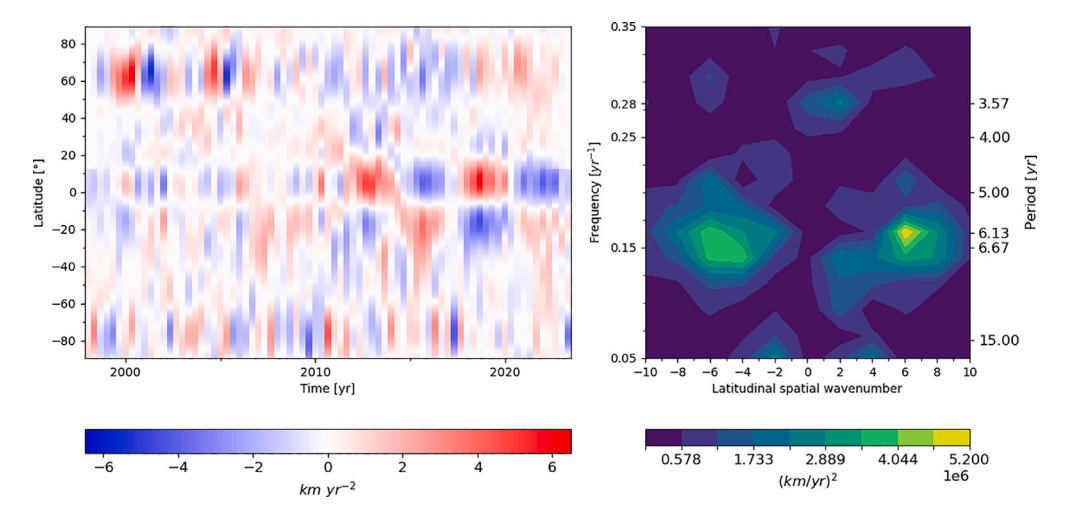


Fig. 12. Left-hand side: time-latitude section of the azimuthal core surface flow acceleration at 170° E. Right-hand side: corresponding power spectral density. Negative peaks indicate northward propagation of energy, positive peaks southward. The peaks at wavenumbers ± 6 correspond to a latitudinal length scale of around 30° or ~ 1825 km, using an outer core radius of 3486 km.

signals as well as quiet zones; however, the locations of the features both in longitude and in time are different from those we observe. The patterns obtained by Gillet et al. (2024) occur at similar longitude ranges, but their Pacific pattern appears earlier than ours and they do not observe the quiescent strip centred on 200°E. Rogers et al. (2025) do find such a quiescent strip, but it is located further to the west than ours. Considering a periodic variation for which $du/dt = \omega u$, where ω is angular frequency, and taking a period of about six years, corresponding to ω of approximately one, the amplitudes of our acceleration disturbances should match those of the velocity disturbances reported by those two studies, which we find to be the case at approximately 5 km yr $^{-2}$ and 5 km yr $^{-1}$ respectively.

The time evolution of the PSD at 10°N (Fig. 11) showed changes both in shape and amplitude. These changes are likely to be reflecting the increase in data availability and quality over time that was noted when comparing the SV data and their flow predictions. Signals in the last 2 time windows in Fig. 11 are more focused on the spectral peaks than those early on; they are also, in shape, more similar to those found by Whaler et al. (2022), suggesting that this is what the signal might look like over the entire time span studied, if data at the earlier times were not degraded, which is causing lateral broadening of the peaks and smearing of power into higher frequencies.

Meridional low-latitude waves vary strongly locally, as shown in Figure A.1. Matching the spatial distribution of signals in the longitude-time section in Fig. 9, we see coherent, focused signals over the west Pacific and the Atlantic region. At other locations, weaker or no signals at all appear.

In the time-latitude section at 170°E (Fig. 12) and the longitudetime sections in the left-hand panels of Fig. 10, we observe a region of alternating positive and negative acceleration at around 60°N with a period of around 3.5 years, which is particularly pronounced between approximately 1999 and 2007 (left-hand panels of Fig. 10). The regional variations of the latitude-time section (see supplementary material Figure A.1) and the top panel of Fig. 12 show that this highlatitude signal does not appear over the whole CMB but rather only in the region underneath Alaska. Istas et al. (2023) calculate a power spectrum of the azimuthal acceleration which show peaks at 3.5 years, with power concentrated at the equator and slightly polewards of the intersection of the tangent cylinder with the core surface (i.e. higher latitude than the northern hemisphere peak found here). These signatures can also be seen in their azimuthal flow. Gillet et al. (2024) also identify a 3.5 year azimuthal flow period, but concentrated at low latitudes. Similar high-latitude variability over the Alaska region has been identified before in models of the SA (Chi-Durán et al., 2020,

2021). Chi-Durán et al. (2021) interpret a series of alternating-sign westward-travelling SA patches at high latitudes as the signatures of zonal MAC waves, but their observed period of 20 years is significantly longer than we are able to resolve.

In the longitude-time section at 10°N (Fig. 9) and in the longitudinal variations of the latitude-time sections and corresponding PSDs (Figure A.1), the azimuthally propagating signals appear at different times in different regions; first, under the Atlantic hemisphere between 2005 and 2017, then under the Pacific hemisphere, starting around 2012. A similar spatio-temporal distribution of westward propagating features was found by Ropp and Lesur (2023) in their core surface flow model: azimuthal velocity variations travel westwards under the Atlantic and under the Pacific hemisphere, and westward propagation of features underneath the Atlantic is confined to the time interval between 2005 and 2015.

The acceleration polarity switches every ~3 years, similar to the time interval between recent successive geomagnetic jerks. Systematic correlations between sign changes in the core surface flow acceleration and the occurrence of geomagnetic jerks have previously been suggested by e.g. Torta et al. (2015), Kloss and Finlay (2019), Aubert and Finlay (2019), Whaler et al. (2022), and Madsen et al. (2025). Patterns in the geomagnetic and flow acceleration at the CMB linked to geomagnetic jerks, such as alternating sign changes, have been connected to the arrival of quasi-geostrophic Magneto-Coriolis waves from deeper inside the outer core (e.g. Aubert et al., 2022; Gillet et al., 2022), which in simulations have sometimes originated as quasi-geostrophic Alfvén waves triggered deep within the outer core (Aubert and Finlay, 2019; Aubert et al., 2022; Finlay et al., 2023).

Signatures of azimuthally drifting features in the core surface flow similar to those we identify in flow acceleration have been observed before: Gillet et al. (2022) identified low-latitude, high-amplitude core flow velocity features drifting westwards in longitude-time and time-latitude sections. They interpret these features as signatures of the aforementioned Magneto-Coriolis waves. Their inferred dominant wavenumber, −2, wave period of ~7 years, and estimate of the propagation velocity of 1500 km yr⁻¹ match our results well. The morphologies of their signals, again in longitude-time and time-latitude plots, resemble ours closely, too, with the exception that their flow was constrained to favour equatorial symmetry and (in their time-latitude diagram,) the signal is more strongly confined to the equator than ours. It should be noted, though, that whereas we have taken the time-derivative of our flows to reveal core-surface waves (a method that preferentially highlights shorter periods, thus acting as a linear highpass filter), Gillet et al. (2022) obtain their signals by bandpass-filtering the flow. Lastly,

interestingly, the timings of sign changes of the high-amplitude flow features found by Gillet et al. (2022) correlate well with the times of maximum azimuthal acceleration amplitude, as one would expect for a normal relationship between flow velocity and acceleration.

In order to classify waves in the outer core, different properties such as their periods and the ratio of magnetic to kinetic energy content have been employed (e.g. Gillet et al., 2022). Although that is not possible here, the similarities in signal morphology, wavenumbers, and period suggest they are signatures of the same wave type inferred by Gillet et al. (2022).

5. Conclusion and outlook

We inverted SV data from ground observatories and satellites for minimally time-varying core surface advective flow over the last 25 years, during which high quality vector low-Earth orbit satellite data are available. The flow model leads to a good fit to the data, with no obvious bias or difference between ability to fit the data from the different sources. It shows the dominant eccentric planetary gyre seen in previous studies. Temporal changes are small by design, but we find that the jet beneath the Bering Strait forming part of the gyre accelerates over the period studied (by about 0.5 km yr $^{-2}$; see Supplementary Information), and the flow changes direction beneath the western Pacific Ocean around 2010 from westward to eastward, in agreement with previous models.

Flow acceleration was calculated by simply first differencing the flow, without smoothing or filtering. Its azimuthal component is consistent with low latitude fast waves, contributing to a growing body of evidence for the existence of such waves in the outer core. They propagate predominantly westward, at low wavenumbers, 6–7 year period, and speeds of order 1500 kmyr⁻¹, sharing their features with magneto-Coriolis waves identified by Gillet et al. (2022). These patterns are visible by eye in longitude-time plots since around 2010, but power spectral density plots identify the features throughout the period studied. Whether their weaker manifestation at earlier epochs reflects a change in flow morphology or arises from the lower density of data available is unknown. Power spectral density plots of time-latitude sections suggest a standing wave, with larger (~6) wavenumbers but a similar period, these wavenumbers correspond to latitudinal angular length scales of approximately 30°.

Pulses of flow acceleration coincide with times and locations where geomagnetic jerks have been identified in SV records, and the times between acceleration peaks are similar to the time between jerks. Further work is required to explore this potential link further.

The continuation of the Swarm mission, the launch of the MSS-1 satellite in a low inclination orbit which is already providing new high quality data at low latitudes (Yao et al., 2025), and the prospect of further additions to the satellite constellation from additional MSS satellites and NanoMagSat (Deconinck et al., 2025), will provide a longer timeline of global data that will enable more robust descriptions and classification of wave signatures, and their relationship to dynamo processes operating in the outer core.

CRediT authorship contribution statement

Carla R. Grüne: Writing – review & editing, Writing – original draft, Visualization, Validation, Software, Methodology, Investigation, Formal analysis, Conceptualization. Kathryn A. Whaler: Writing – review & editing, Writing – original draft, Validation, Supervision, Software, Project administration, Methodology, Investigation, Funding acquisition, Formal analysis, Conceptualization. Frederik Dahl Madsen: Writing – original draft, Visualization, Validation, Supervision, Software, Project administration, Methodology, Investigation, Formal analysis, Data curation, Conceptualization.

Declaration of competing interest

The authors declare that they have no known competing financial interests or personal relationships that could have appeared to influence the work reported in this paper.

Acknowledgements

Awards from the Royal Astronomical Society and University of Edinburgh School of GeoSciences enabled CG to present this research at the Swarm 10 Year Anniversary and Science Conference, which prompted a number of useful comments and discussions. KAW was supported partly by ESA through the Swarm DISC activities, funded by ESA contract no. 4000109587. FDM was supported by a NERC Doctoral Training Partnership grant (NE/S007407/1) and in part funded by BGS University Funding Initiative Ph.D. studentship S493. The results presented here include data collected at magnetic observatories. We thank the national institutes that support them and INTERMAGNET for promoting high standards of magnetic observatory practice (www. intermagnet.org). We thank DTU for processing the satellite data and preprocessing the ground observatory data for our purposes. Swarm GVO data were obtained from the DISC server. GVO data from Ørsted, CHAMP, and CryoSat-2 were provided by DTU. We thank Mathieu Dumberry and an anonymous reviewer for insightful comments that have improved this manuscript.

Appendix A. Supplementary data

Supplementary material related to this article can be found online at https://doi.org/10.1016/j.pepi.2025.107435.

Data availability

All data are available online, and appropriately referenced in the manuscript.

References

- Alfvén, H., 1942. Existence of Electromagnetic-Hydrodynamic waves. Nature 150, 405–406. http://dx.doi.org/10.1038/150405d0.
- Amit, H., Olson, P., 2004. Helical core flow from geomagnetic secular variation. Phys. Earth Planet. Inter. 147, 1–25.
- Aubert, J., Finlay, C.C., 2019. Geomagnetic jerks and rapid hydromagnetic waves focusing at Earth's core surface. Nat. Geosci. 12, 393–398. http://dx.doi.org/10. 3810/s41561-019-0355-1.
- Aubert, J., Gillet, N., 2021. The interplay of fast waves and slow convection in geodynamo simulations nearing earth's core conditions. Geophys. J. Int. 225, 1854–1873. http://dx.doi.org/10.9310/gji/ggab054.
- Aubert, J., Livermore, P.W., Finlay, C.C., Fournier, A., Gillet, N., 2022. A taxonomy of simulated geomagnetic jerks. Geophys. J. Int. 231, 650–672. http://dx.doi.org/10. 9310/gji/ggac212.
- Baerenzung, J., Holschneider, M., Lesur, V., 2016. The flow at the Earth's coremantle boundary under weak prior constraints. J. Geophys. Res.: Solid Earth 121, 1343–1364. http://dx.doi.org/10.0210/2015JB012464.
- Bärenzung, J., Holschneider, M., Wicht, J., Sanchez, S., Lesur, V., 2018. Modeling and predicting the short-term evolution of the geomagnetic field. J. Geophys. Res.: Solid Earth 123, 4539–4560.
- Barrois, O., Gillet, N., Aubert, J., 2017. Contributions to the geomagnetic secular variation from a reanalysis of core surface dynamics. Geophys. J. Int. 211, 50–68.
- Beggan, C., Whaler, K., 2008. Core flow modelling assumptions. Phys. Earth Planet. Inter. 167, 217–222. http://dx.doi.org/10.1016/J.PEPI.2008.04.011.
- Beggan, C.D., Whaler, K.A., 2009. Forecasting change of the magnetic field using core surface flows and ensemble Kalman filtering. Geophys. Res. Lett. 36 (2009), GL039927. URL https://agupubs.onlinelibrary.wiley.com/doi/10.1029/2009GL039927.
- Bloxham, J, 1988. The Determination of Fluid Flow At the Core Surface from Geomagnetic Observations. Springer Netherlands, Dordrecht, pp. 189–208. http://dx.doi.org/10.1007/978-94-009-2857-2_9.
- Bloxham, J., 1992. The steady part of the secular variation of the Earth's magnetic field. J. Geophys. Res.: Solid Earth 97, 19565–19579.

- Bloxham, J., Jackson, A., 1991. Fluid flow near the surface of Earth's outer core. Rev. Geophys. 29, 97–120, URL https://agupubs.onlinelibrary.wiley.com/doi/10.1029/90RG02470.
- Buffett, B., 2014. Geomagnetic fluctuations reveal stable stratification at the top of the Earth's core. Nature 507, 484–487. http://dx.doi.org/10.1038/nature13122.
- Buffett, B., Knezek, N., Holme, R., 2016. Evidence for MAC waves at the top of Earth's core and implications for variations in length of day. Geophys. J. Int. 204, 1789–1800. http://dx.doi.org/10.1093/gji/ggv552.
- Chi-Durán, R., Avery, M.S., Buffett, B.A., 2021. Signatures of high-latitude waves in observations of geomagnetic acceleration. Geophys. Res. Lett. 48, e2021GL094692. http://dx.doi.org/10.1029/2021GL094692.
- Chi-Durán, R., Avery, M.S., Knezek, N., Buffett, B.A., 2020. Decomposition of geomagnetic secular acceleration into traveling waves using complex empirical orthogonal functions. Geophys. Res. Lett. 47, e2020GL087940. http://dx.doi.org/10.1029/2020GL087940.
- Chulliat, A., Maus, S., 2014. Geomagnetic secular acceleration, jerks, and a localized standing wave at the core surface from 2000 to 2010. J. Geophys. Res.: Solid Earth 119, 1531–1543. http://dx.doi.org/10.1002/2013JB010604.
- Chulliat, A., Thébault, E., Hulot, G., 2010. Core field acceleration pulse as a common cause of the 2003 and 2007 geomagnetic jerks. Geophys. Res. Lett. 37, http://dx.doi.org/10.1029/2009GL042019.
- Courtillot, V., Mouël, J.Le., 1984. Geomagnetic secular variation impulses. Nature 311, 709–716. http://dx.doi.org/10.1038/311709a0.
- Deconinck, F., Hulot, G., Léger, J.M., Clausen, L.B.N., Pastena, M., Lejault, J.P., Wilkinson, J., Caballero, D.M., Tostado, M.V., Coïsson, P., Jager, T., Nieto, P., Jørgensen, J.L., 2025. NanoMagSat status: a 3x16u low-earth orbit constellation to monitor the earth magnetic field and the ionospheric environment. In: Petrozzillstad, M. (Ed.), Small Satellites Systems and Services Symposium (4S 2024). International Society for Optics and Photonics. SPIE., p. 135462K. http://dx.doi.org/10.111710/12.3062471.
- Eymin, C., Hulot, G., 2005. On core surface flows inferred from satellite magnetic data. Phys. Earth Planet. Inter. 152, 200–220.
- Finlay, C.C., 2005. Hydromagnetic Waves in Earth's Core and their Influence on Geomagnetic Secular Variation. (Ph.D. thesis). University of Leeds.
- Finlay, C C, 2008. Course 8 waves in the presence of magnetic fields. Rotat. Convect. URL https://www.sciencedirect.com/science/article/pii/S0924809908800121.
- Finlay, C.C., Gillet, N., Aubert, J., Livermore, P.W., Jault, D., 2023. Gyres, jets and waves in the earth's core. Nat. Rev. Earth & Environ. 4, 377–392, URL https://www.nature.com/articles/s43017-023-00425-w.
- Finlay, C.C., Kloss, C., Olsen, N., Hammer, M.D., Tøffner-Clausen, L., Grayver, A., Kuvshinov, A., 2020. The CHAOS-7 geomagnetic field model and observed changes in the south atlantic anomaly. Earth, Planets Space 72 (156), http://dx.doi.org/10. 1186/s40623-020-01252-9.
- Friis-Christensen, E., Lühr, G., 2006. Swarm: A constellation to study the Earth's magnetic field. Earth, Planets Space 58, 351–358. http://dx.doi.org/10.118610/ BF03351933.
- Gerick, F., Jault, D., Noir, J., 2021. Fast quasi-geostrophic Magneto-coriolis modes in the earth's core. Geophys. Res. Lett. 48, e2020GL090803. http://dx.doi.org/10. 2910/2020GL090803.
- Gillet, N., Dall'Asta, F., Amblard, P.O., Claveau, R., Aubert, J., 2024. Waves in Earth's core and geomagnetic field forecast. Phys. Earth Planet. Inter. 357, 107284.
- Gillet, N., Gerick, F., Jault, D., Schwaiger, T., Aubert, J., Istas, M., 2022. Satellite magnetic data reveal interannual waves in Earth's core. Proc. the Natl. ACademy Sci. 119, e2115258119. http://dx.doi.org/10.7310/pnas.2115258119.
- Gillet, Z., Huder, L., Aubert, J., 2019. A reduced stochastic model of core surface dynamics based on geodynamo simulations. Geophys. J. Int. 219, 522–539. http://dx.doi.org/10.1093/gji/ggz313, arXiv:https://academic.oup.com/gji/article-pdf/219/1/522/28984585/ggz313.pdf.
- Gillet, N., Jault, D., Finlay, C.C., 2015. Planetary gyre, time-dependent eddies, torsional waves, and equatorial jets at the earth's core surface. J. Geophys. Res.: Solid Earth 120, 3991–4013. http://dx.doi.org/10.1002/2014JB011786.
- Gubbins, D., Roberts, P.H., 1987. Magnetohydrodynamics of the earth's core, In: Jacobs, J.A. (Ed.), first ed. In: Geomagnetism, vol. 2, Academic Press, pp. 1–183.
- Hammer, M.D., Cox, G.A., Brown, W.J., Beggan, C.D., Finlay, C.C., 2021. Geomagnetic virtual observatories: monitoring geomagnetic secular variation with the swarm satellites. Earth. Planets Space 73 (54), http://dx.doi.org/10.1186/s40623-021-01357-9.
- Holme, R., 2015. 8.04 large-scale flow in the core. In: Schubert, G. (Ed.), Treatise on Geophysics (Second Edition), second ed. Elsevier, Oxford, pp. 91–113, URL https://www.sciencedirect.com/science/article/pii/B978044453802400138X.
- Istas, M., Gillet, N., Finlay, C., Hammer, M., Huder, L., 2023. Transient core surface dynamics from ground and satellite geomagnetic data. Geophys. J. Int. 233, 1890–1915.
- Jackson, A., 1997. Time-dependency of tangentially geostrophic core surface motions. Phys. Earth Planet. Inter. 103, 293–311, URL https://www.sciencedirect.com/science/article/pii/S0031920197000393.
- Jackson, A., Finlay, C., Schubert, G., 2015. 5.05- geomagnetic secular variation and its applications to the core. Treatise Geophys. 2, 137–184. http://dx.doi.org/10.1016/ B978-0-444-53802-4.00099-3.

- Jault, D., Finlay, C.C., 2015. 8.09 waves in the core and mechanical core-mantle interactions. URL https://www.sciencedirect.com/science/article/pii/ B9780444538024001500.
- Jault, D., Gire, C., Le Mouel, J.L., 1988. Westward drift, core motions and exchanges of angular momentum between core and mantle. Nature 333, 353–356. http: //dx.doi.org/10.1038/333353a0.
- Kloss, C., Finlay, C.C., 2019. Time-dependent low-latitude core flow and geomagnetic field acceleration pulses. Geophys. J. Int. 217, 140–168. http://dx.doi.org/10.1093/ gji/ggy545.
- Lesur, V., Gillet, N., Hammer, M., Mandea, M., 2022. Rapid variations of Earth's core magnetic field. Surv. Geophys. 43, 41–69. http://dx.doi.org/10.1007/s10712-021-0005004.
- Lesur, V., Wardinski, I., Asari, S., Minchev, B., Mandea, M., 2010. Modelling the Earth's core magnetic field under flow constraints. Earth, Planets Space 62, 503–516. http://dx.doi.org/10.5047/eps.2010.02.010.
- Lesur, V., Whaler, K., Wardinski, I., 2015. Are geomagnetic data consistent with stably stratified flow at the core-mantle boundary? Geophys. J. Int. 201, 929–946. http://dx.doi.org/10.1093/gji/ggv031.
- Li, J., Lin, Y., Zhang, K., 2024. Dynamic mode decomposition of the core surface flow inverted from geomagnetic field models. Geophys. Res. Lett. 51, e2023GL106362. http://dx.doi.org/10.2910/2023GL106362.
- Livermore, P.W., Hollerbach, R., Finlay, C.C., 2017. An accelerating high-latitude jet in Earth's core. Nat. Geosci. 10, 62–68. http://dx.doi.org/10.1038/ngeo2859.
- Madsen, F.D., Whaler, K.A., Beggan, C.D., Brown, W.J., Lauridsen, J.B., Holme, R., 2025. Modelling geomagnetic jerks with core surface flow derived from satellite gradient tensor elements of secular variation. Phys. Earth Planet. Inter. 366, 107336, URL https://www.sciencedirect.com/science/article/pii/S0031920125000305.
- Malin, S., Hodder, B., 1982. Was the 1970 geomagnetic jerk of internal or external origin? Nature 296, 726–728.
- Mandea, M., Bellanger, E., Le Mouël, J.L., 2000. A geomagnetic jerk for the end of the 20th century? Earth Planet. Sci. Lett. 183, 369–373. http://dx.doi.org/10.1016/ S0012-821X(00)00284-3.
- Mandea, M., Olsen, N., 2006. A new approach to directly determine the secular variation from magnetic satellite observations. Geophys. Res. Lett. 33, http://dx. doi.org/10.1029/2006GL026616.
- More, C., Dumberry, M., 2018. Convectively driven decadal zonal accelerations in Earth's fluid core. Geophys. J. Int. 213, 434–446.
- Olsen, N., Lühr, H., Finlay, C.C., Sabaka, T.J., Michaelis, I., Rauberg, J., Tøffner-Clausen, L., 2014. The CHAOS-4 geomagnetic field model. Geophys. J. Int. 197, 815–827.
- Olsen, N., Mandea, M., 2007. Investigation of a secular variation impulse using satellite data: The 2003 geomagnetic jerk. Earth Planet. Sci. Lett. 255, 94–105. http://dx.doi.org/10.1016/j.epsl.2006.12.008.
- Pais, M., Jault, D., 2008. Quasi-geostrophic flows responsible for the secular variation of the Earth's magnetic field. Geophys. J. Int. 173, 421–443. http://dx.doi.org/10. 1111/j.1365-246X.2008.03741.x.
- Pavón-Carrasco, F.J., Marsal, S., Campuzano, S.A., Torta, J.M., 2021. Signs of a new geomagnetic jerk between 2019 and 2020 from swarm and observatory data. Earth, Planets Space 73 (175), http://dx.doi.org/10.1186/s40623-021-01504-2.
- Pinheiro, K., Amit, H., Terra-Nova, F., 2019. Geomagnetic jerk features produced using synthetic core flow models. Phys. Earth Planet. Inter. 291, 35–53. http://dx.doi.org/10.1016/j.pepi.2019.03.006.
- Pinheiro, K., Jackson, A., 2008. Can a 1-D mantle electrical conductivity model generate magnetic jerk differential time delays?. Geophys. J. Int. 173, 781–792. http://dx.doi.org/10.1111/j.1365-246X.2008.03762.x.
- Pinheiro, K., Jackson, A., Finlay, C., 2011. Measurements and uncertainties of the occurrence time of the 1969 1978, 1991, and 1999 geomagnetic jerks. Geochem. Geophys. Geosystems 12, http://dx.doi.org/10.1029/2011GC003706.
- Roberts, P., Scott, S., 1965. On analysis of the secular variation 1. a hydromagnetic constraint: theory. J. Geomagn. Geoelectr. 17, 137–151. http://dx.doi.org/10.5636/ igg.17.137.
- Rogers, H.F., Gillet, N., Aubert, J., Personnettaz, P., Mandea, M., 2025. Effects of geodynamo priors and geomagnetic data on inverted core surface flows. Phys. Earth Planet. Inter. 364, 107323, URL https://www.sciencedirect.com/science/article/ pii/S0031920125000172.
- Ropp, G., Lesur, V., 2023. Mid-latitude and equatorial core surface flow variations derived from observatory and satellite magnetic data. Geophys. J. Int. 234, 1191–1204. http://dx.doi.org/10.1093/gji/ggad113.
- Schwaiger, T., Gillet, N., Jault, D., Istas, M., Mandea, M., 2024. Wave-like motions and torques in Earth's core as inferred from geomagnetic data: A synthetic study. Phys. Earth Planet. Inter. 346, 107104. http://dx.doi.org/10.1016/J.PEPI.2023.107104.
- Suttie, N., Nilsson, A., Gillet, N., Dumberry, M., 2025. Large-scale palaeoflow at the top of Earth's core. Earth Planet. Sci. Lett. 652, 119185. http://dx.doi.org/10.1016/J. EPSL.2024.119185.
- Torta, J.M., Pavón-Carrasco, F.J., Marsal, S., Finlay, C.C., 2015. Evidence for a new geomagnetic jerk in 2014. Geophys. Res. Lett. 42, 7933–7940. http://dx.doi.org/ 10.1002/2015GL065501.
- Tsang, Y.K., Jones, C.A., 2024. Scaling of the geomagnetic secular variation timescale. Geophys. J. Int. 239, 1–16.

- Whaler, K., 1980. Does the whole of the earth's core convect? Nature 287, 528–530. http://dx.doi.org/10.1038/287528a0.
- Whaler, K., 1986. Geomagnetic evidence for fluid upwelling at the core-mantle boundary. Geophys. J. Int. 86, 563–588. http://dx.doi.org/10.1111/j.1365-246X. 1986.tb03844.x.
- Whaler, K.A., Hammer, M.D., Finlay, C.C., Olsen, N., 2022. Core surface flow changes associated with the 2017 Pacific geomagnetic jerk. Geophys. Res. Lett. 49, e2022GL098616, URL https://agupubs.onlinelibrary.wiley.com/doi/10.1029/ 2022GL098616.
- Whaler, K., Olsen, N., Finlay, C., 2016. Decadal variability in core surface flows deduced from geomagnetic observatory monthly means. Geophys. J. Int. 207, 228–243. http://dx.doi.org/10.1093/gji/ggw268.
- Wheeler, M., Kiladis, G.N., 1999. Convectively coupled equatorial waves: Analysis of clouds and temperature in the wavenumber–frequency domain. J. Atmos. Sci. 56, 374–399. http://dx.doi.org/10.117510/1520-0469(1999)056<0374:CCEWAO> 2.0.CO;2.
- Yao, H., Xu, J., Zhang, K., 2025. A method for simultaneously determining Earth's magnetic field and mantle conductivity models using MSS-1 and Swarm satellite magnetic data. Phys. Earth Planet. Inter. 358, 107296.